KeAi
CHINESE ROOTS
GLOBAL IMPACT

Contents lists available at ScienceDirect

Petroleum Science





Original Paper

An integrated multi-scale approach for transient analysis of multi-well horizontal pad with well interference in shale gas reservoirs: Methodology and case study



Hong-Yang Chu ^{a, b, c, *}, Si-Dong Fang ^a, Zhi-Qiang Ren ^{b, **}, Jian-Dong Zou ^d, Ran Bi ^e, Wei-Yao Zhu ^b, W. John Lee ^c

- ^a State Key Laboratory of Shale Oil and Gas Enrichment Mechanisms and Effective Development, Beijing, 102206, China
- ^b School of Civil and Resources Engineering, University of Science and Technology Beijing, 100083, Beijing, China
- ^c Harold Vance Department of Petroleum Engineering, Texas A&M University, 77843, College Station, USA
- d Research Institute of Exploration and Development, Changaing Oilfield Company, PetroChina, Xi'an, 710018, Shaanxi, China
- ^e Research Institute of Petroleum Exploration and Development, PetroChina, Beijing, 100083, China

ARTICLE INFO

Article history: Received 19 February 2024 Received in revised form 21 December 2024 Accepted 22 December 2024 Available online 25 December 2024

Edited by Yan-Hua Sun

Keywords: Multi-well horizontal pad Well interference Shale gas reservoir Multi-scale approach Transient analysis

ABSTRACT

Shale gas, as a clean, low-carbon, and abundant unconventional natural gas resource, plays a crucial role in achieving clean energy transformation and carbon neutrality. The Fuling shale gas reservoir in Sichuan Basin stands out as China's most promising area for shale gas exploration and recovery. However, the continuous recovery of shale gas in the southern Sichuan Basin has led to well interference events in hundreds of wells, with the furthest well distance reaching over 2000 m. This study introduces a multiscale approach for transient analysis of a multi-well horizontal pad with well interference in shale gas reservoirs. The approach utilizes Laplace transform technology, boundary element theory, and the finite difference method to address the complexities of the system. Well interference is managed using the pressure superposition principle. To validate the proposed multi-scale method, a commercial numerical simulator is employed. The comprehensive pressure behavior of a multi-well horizontal pad in a shale gas reservoir is analyzed, encompassing wellbore storage effect, skin effect, bilinear flow, linear flow, pseudo-radial flow of primary fractures, well interference period, dual-porosity flow, pseudo-radial flow of the total system, and boundary-dominated flow. A case study is conducted on the typical well, the well with the longest production history in the Fuling shale gas reservoir. The rate transient analysis is conducted to integrate up to 229 days of shale gas production daily data and wellhead pressure data, enabling the generation of pressure behavior under unit flow rate. The results indicate that the linear flow, transitional flow, and boundary-dominated flow are more likely to be observed in the actual data. Secondary fractures are considered to be the primary pathways for fluid migration during well interference events. The evaluated formation permeability is 2.58×10^{-2} mD, the well spacing is 227.8 m, the diffusion coefficient is 1.49×10^{-4} , and the skin factor is 0.09.

© 2024 The Authors. Publishing services by Elsevier B.V. on behalf of KeAi Communications Co. Ltd. This is an open access article under the CC BY license (http://creativecommons.org/licenses/by/4.0/).

1. Introduction

Natural gas is both efficient and clean, and it has a crucial role to play in the ongoing energy transformation process. According to data from 2022, China's natural gas production and consumption

E-mail addresses: hongyangchu@126.com (H.-Y. Chu), q2140806816@163.com (Z.-O. Ren).

levels reached 2177.9 \times 10⁸ m³ and 3663 \times 10⁸ m³, respectively. However, over 40% of this natural gas is imported from abroad, and China's energy demand continues to outstrip its production (Zou et al., 2020). With conventional natural gas resources gradually being depleted (Kanwal et al., 2022; Jin, 2023), attention has increasingly turned to shale gas as an unconventional resource with abundant reserves (Chu et al., 2023a; Ehlig-Economides and de Guzman, 2020). The Energy Information Administration (EIA) reports that global shale gas reserves total approximately 456×10^{12} m³, with China accounting for 24.66% of this total.

The shale gas reservoirs are characterized by low permeability

^{*} Corresponding author.

^{**} Corresponding author.

and porosity, and a complex pore structure (Taghavinejad et al., 2020). Consequently, hydraulic fracturing and horizontal drilling techniques are commonly employed for shale gas recovery (Abdelaziz et al., 2023; Cui et al., 2023; Bellani et al., 2021). The hydraulic fracturing process creates a primary fracture system, establishing flow channels through which shale gas can enter the wellbore (Thomas et al., 2019). These channels are interconnected with the matrix system via natural fractures. The flow domain of shale gas reservoirs comprises various structures, such as micronano pores, micro-fractures, secondary fractures, and primary fractures (Arif et al., 2021; Kurotori et al., 2023). Under the influence of pressure and concentration differences, shale gas exhibits multiscale flow as it traverses the intricate matrix-fracture system (Micheal et al., 2021; Takbiri-Borujeni et al., 2019). Moreover, the implementation of a multi-well horizontal pad is an engineering approach aimed at reducing costs and increasing gas production in shale gas recovery (Sherratt et al., 2021). It is crucial to consider the impact of well interference on shale gas production due to the reduced well spacing associated with the multi-well horizontal pad (Altman et al., 2020). Considering these factors, this paper primarily focuses on reviewing the challenges of multi-scale flow and well interference during shale gas production.

(1) Multi-scale flow

During shale gas production, the pressure in reservoirs begins to decrease at the micro- and nanoscale (Chen et al., 2015). Shale gas molecules on the surface of organic matter migrate from the matrix to microscopic fractures following Knudsen diffusion law. Adsorbed gas gradually desorbs in accordance with Langmuir's law (Yang and Liu, 2020). To classify shale gas flow, Singh and Javadpour (2016) categorized it into continuous flow (0 < Kn < 0.001), slip flow (0.001 < Kn < 0.1), transition flow (0.1 < Kn < 10), and free flow of molecules in the matrix (Kn > 10). When Kn > 0.001, Fick's law is employed instead of Darcy's law to more accurately describe the microscale shale gas flow (Taghavinejad et al., 2020).

On a macro scale, primary fractures and some secondary fractures form an asymmetrical large-scale complex hydraulic fracture area (Damjanac et al., 2020). Considering the multi-scale challenges posed by this complex fracture area, continuous multi-medium models and discrete models are currently employed (Farah and Delorme, 2020). The continuous multi-medium model is widely used as it comprehensively accounts for the interaction between micro- and macro-scales (Soulaine et al., 2019). Micheal et al. (2022) established a quadruple continuum model that includes kerogen, inorganic matrix systems, natural fractures, and hydraulic fracture systems, while considering stress sensitivity and multiple physical fields. Sobecki et al. (2020) combined a developed pore size distribution amplification method with a triple porous medium model consisting of small pores, large pores, and fractures to represent different pore sizes within the matrix. Dahim et al. (2020), using a semi-analytical method, developed a triple porous medium model comprising the matrix, natural fractures, and adsorbed gas for two-phase flow.

Although discrete models offer higher simulation accuracy, they suffer from low computational efficiency (Zhu et al., 2023; Chen et al., 2021). Torres et al. (2021) utilized an embedded discrete fracture model to characterize natural fractures in the Eagle Ford Formation and coupled fracture propagation simulators. To mitigate calculation errors associated with explicit methods, Du et al. (2021) proposed a fully implicit and coupled discrete fracture model for deformable rock in shale gas reservoirs. These valuable approaches provide guidance for the study of multi-scale flow in shale gas reservoirs.

(2) Well interference

The economic benefits of shale gas recovery can be enhanced by implementing a multi-well horizontal pad. However, it is crucial to consider the presence of well interference. Well interference can occur in various forms, including direct fracture hits or overlapping of stimulated reservoir volumes (SRVs), as well as pressure interference through natural fractures and conductive faults (Al-Shami et al., 2023). As the studied basins differ, well interference has both positive effects on production from the Haynesville and Bakken reservoirs, and negative impacts on production from the Woodford and Niobrara formations (Miller et al., 2016). To address these various interference issues in shale gas reservoirs, scholars have proposed analytical methods, semi-analytic methods, and numerical methods (Chu et al., 2023b; Coley et al., 2023; Molina, 2019; Rivera and Shin, 2023; Wang et al., 2021; Yang et al., 2020).

In terms of analytical methods, Haghshenas and Qanbari (2021) developed a coupled gas flow model to study the pressure interference process between fractures and the matrix. Ozkan (2023) conducted simulations on two parallel fractured horizontal wells in an unconventional reservoir to evaluate well interference by dividing the one-dimensional flow blocks based on the trilinear flow hypothesis. Liu et al. (2020) utilized semi-analytic theory to simulate the well interference resulting from fracture hits in a parent and child well system. Hamdi et al. (2021) introduced a semi-analytical method using a communicating tanks model and macroscopic material balance to quantitatively analyze interference in multi-well horizontal pads through online production data from individual shale gas wells.

For numerical simulation methods, Zheng et al. (2020) established a numerical model that couples fracturing fluid flow with rock deformation to investigate the influence of multi-well interference on the dynamic propagation of fractures. Fiallos et al. (2019), combining an embedded discrete fracture model with a compositional model, studied the impact of connecting fracturesled well interference through multi-well history matching.

The aforementioned studies of well interference provide a foundation for improving shale gas recovery. However, these studies have not fully incorporated the effects of gas adsorption, desorption, and multi-scale flow in shale gas reservoirs. Additionally, most existing multi-scale flow models for shale gas are focused on single wells. To address these gaps, this paper takes into account multiple physical mechanisms, including multi-scale flow and well interference, in a comprehensive manner. Initially, the paper employs perturbation transformation and Laplace transformation methods to obtain the point source solutions for the primary fracture, secondary fracture, matrix, and boundary system. The bottom hole pseudo pressure (BHP) is then determined using the Gaussian elimination method. Subsequently, the Stehfest numerical inversion algorithm is applied to consider the influence of wellbore storage and skin effect, enabling the determination of BHP in the time domain. To validate the proposed model, a commercial numerical simulator is utilized. Sensitivity analysis is conducted to examine the impact of key parameters on the pressure behavior of multi-well horizontal pads in shale gas reservoirs. Furthermore, a case study, combined with rate transient analysis, is performed on a typical well in the Fuling shale gas reservoir to demonstrate the practicality of the model.

The innovations of this work are as follows: (1) an integrated multi-scale approach for the transient analysis of multi-well horizontal pads with well interference in shale gas reservoirs is proposed, (2) typical pressure behavior is diagnostically identified to characterize the flow regimes, and (3) the practicality of the method is demonstrated using field data from the Fuling shale gas reservoir.

2. Semianalytical methodology

2.1. Physical model and assumptions

As shown in Fig. 1, the flow in shale gas reservoirs from meso-scale to nanoscale includes Darcy flow, slip flow, and diffusion. Shale gas molecules adhere to the surface of the spherical matrix unit of shales in accordance with the Langmuir adsorption law. The secondary fractures and matrix are modeled as a continuous dual-medium system, and the transportation between the two systems is transient. Primary fractures from multi-well horizontal pads have varying lengths, dip angles, and conductivities. The entire reservoir domain is enclosed by an impermeable and irregular outer boundary, and both the top and bottom interfaces in the vertical direction are also impermeable. The multiple wells in a multi-well horizontal pad are undergoing production. The well interference propagates through various media, including primary fractures, secondary fractures, and the surrounding matrix. The remaining assumptions are as follows.

- (1) Shale gas is a single-phase compressible fluid and follows Darcy's law.
- (2) The impact of gravity and temperature on shale gas flow is neglected.
- (3) The reservoir domain maintains a uniform initial temperature and pressure distribution.
- (4) Fluid flow in primary fractures is one-dimensional along the fracture length.
- (5) The effect of stress sensitivity on permeability is expressed as an exponential function (Pedrosa Jr, 1986).
- (6) The reservoir domain is homogeneous and has a constant formation thickness.

(7) The permeability anisotropy of shale formations can be accounted for using the method proposed by Spivey and Lee (1998).

Although this work is primarily focused on shale reservoirs, the model, based on the continuum media approach proposed by previous works, can be easily applied to carbonate reservoirs (Jalali and Ershaghi, 1987).

2.2. Mathematical model

2.2.1. Primary fracture system

With the equations of motion in Appendix A, the shale gas continuity equation within primary fractures can be given as

$$e^{-\alpha(p_{i}-p)}\left[\alpha'\left(\frac{\partial m_{F}}{\partial r}\right)^{2}+\frac{\partial^{2} m_{F}}{\partial r^{2}}\right]+\frac{2p_{sc}}{k_{Fi}\omega T_{sc}}q_{F}+\frac{2p_{sc}}{k_{Fi}\omega T_{sc}}q_{F}\delta(r)=0$$
(1)

where α is the permeability modulus; α' is the modified permeability modulus; $k_{\rm Fi}$ is the permeability of primary fracture system; ω refers to the fracture width; $p_{\rm sc}$ and $T_{\rm sc}$ are the pressure and temperature at standard conditions; m is the pseudo-pressure; r refers to the radial distance; $q_{\rm F}$ is the flux rate of primary fracture system; subscript F denotes primary fracture; subscript i denotes initial state. Substituting dimensionless values in Appendix B, the dimensionless governing equation within hydraulic fractures can be given as

$$e^{-\alpha_D m_{FD}} \left[\alpha_D \left(\frac{\partial m_{FD}}{\partial r_D} \right)^2 - \frac{\partial^2 m_{FD}}{\partial r_D^2} \right] + \frac{2\pi}{C_{FD}} q_{FD} + \frac{2\pi}{C_{FD}} q_{FD} \delta(r) = 0 \qquad (2)$$

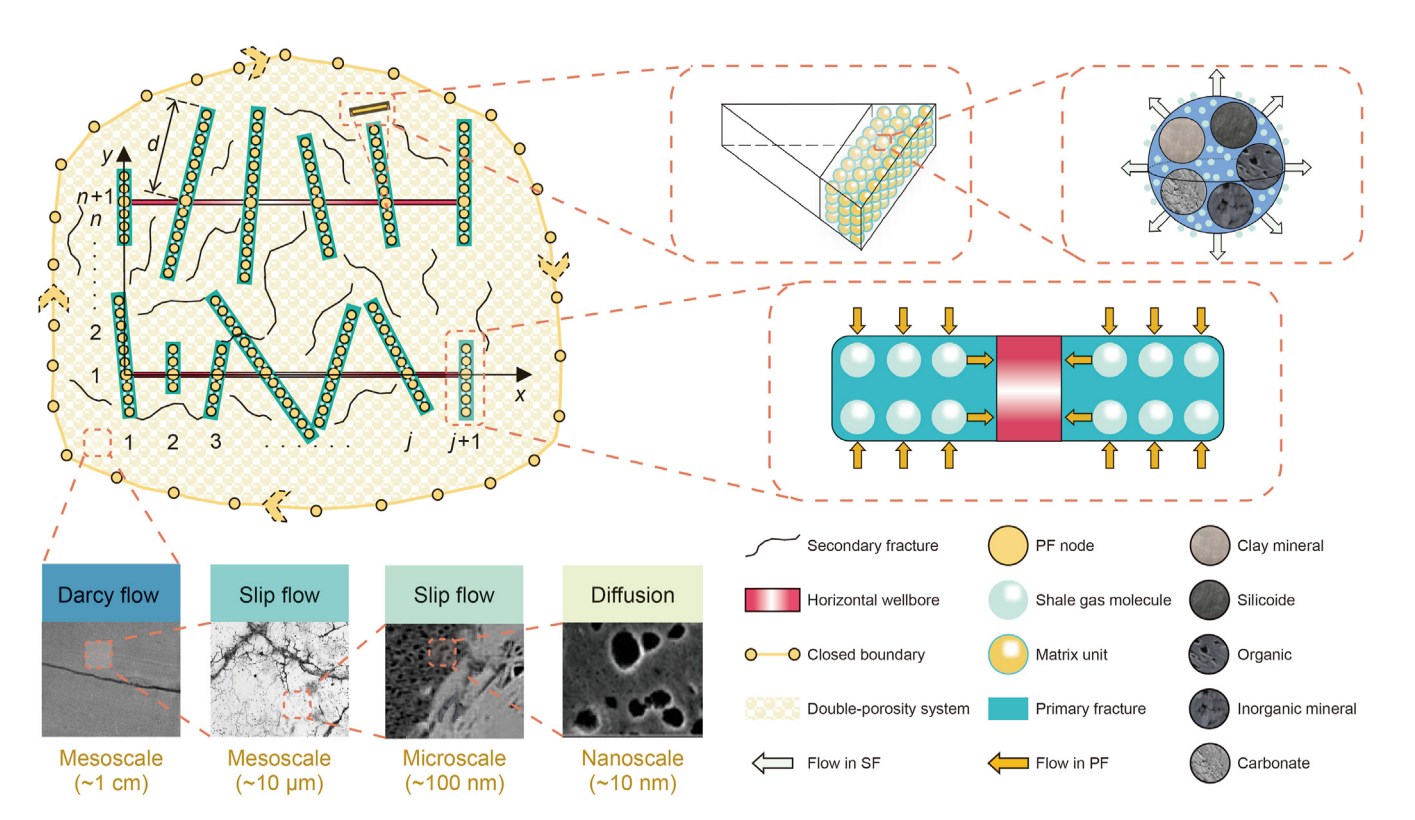


Fig. 1. Physical model of the multi-well horizontal pad with well interference in shale gas reservoirs. The magnified view represents the flow visualization of shale gas molecules within primary fractures, secondary fractures, and the matrix.

where $C_{\rm FD}$ is the dimensionless conductivity of primary fractures; subscript D indicates dimensionless state; $\delta(r)$ is the Dirac delta function. The internal boundary conditions satisfy that the pressure at the fracture heel is equal to the BHP. The shale gas wells are under the control condition of constant rate condition.

$$\lim_{r_{\rm D}\to 0} -e^{-\alpha_{\rm D} m_{\rm FD}} \frac{\partial m_{\rm FD}}{\partial r_{\rm D}} \bigg|_{r_{\rm D}} = \frac{2\pi}{C_{\rm FD}} q_{\rm F,wD} \tag{3}$$

$$\lim_{r_{\rm D} \to 0} m_{\rm FD}|_{r_{\rm D}} = m_{\rm WD} \tag{4}$$

where $q_{\rm F,WD}$ is the dimensionless bottom-hole inflow rate; $m_{\rm WD}$ refers to the dimensionless BHP; subscript w refers to wellbore. The tip of primary fractures is sealed and the fluid transportation between hydraulic fractures and reservoir is considered to be through the sides of the fracture.

$$\left. \frac{\partial m_{\rm FD}}{\partial r_{\rm D}} \right|_{r_{\rm D} = L_{\rm FD}} = 0 \tag{5}$$

where $L_{\rm FD}$ is the dimensionless length of primary fractures. The initial conditions for hydraulic fractures can be given as

$$m_{\rm FD}|_{t_{\rm D}=0}=0$$
 (6)

The nonlinear items and time related items in Eqs. (2) and (3) can be eliminated using perturbation transformation theory (Pedrosa Jr, 1986), and it can be rewritten as

$$\frac{d^{2}\xi_{FD}}{dr_{D}^{2}} - \frac{2\pi}{C_{FD}}q_{FD} - \frac{2\pi}{C_{FD}}\delta(r) = 0 \tag{7}$$

$$\lim_{T_{\rm D} \to 0} \frac{\partial \xi_{\rm FD}}{\partial T_{\rm D}} \bigg|_{T_{\rm c}} = -\frac{2\pi}{C_{\rm FD}} q_{\rm F, wD} \tag{8}$$

where ξ_{FD} is the pressure items after perturbation transformation. Eq. (7) is a reducible second-order partial differential equation, the general solution can be written directly as

$$\xi_{FD}(x_D) = \frac{2\pi}{C_{FD}} \int_{0}^{x_2} \int_{0}^{x_1} q_{FD} dx_1 dx_2 + \int_{0}^{x_2} -\frac{2\pi}{C_{FD}} q_{F,wD} dx_2 + \xi_{wD}$$
 (9)

where x_1 and x_2 are variables of integration. According to the discretization theory of Eq. (9), the dimensionless pseudo-pressure difference between j-th segment on the i-th fracture and BHP can be written as

$$e^{-\alpha(p_{i}-p)} \left(\frac{1}{r} \frac{\partial p^{2}}{\partial r} + \alpha \frac{\partial p}{\partial r} \frac{\partial p^{2}}{\partial r} + \frac{\partial^{2} p^{2}}{\partial r^{2}} + \frac{\partial^{2} p^{2}}{\partial z^{2}} + \alpha \frac{\partial p}{\partial z} \frac{\partial p^{2}}{\partial z} \right)$$

$$= \frac{2\mu ZTp_{sc}}{k_{fi}T_{sc}} \frac{\partial V}{\partial t} + \frac{\mu C_{g} \varphi}{k_{fi}} \frac{\partial p^{2}}{\partial t}$$

$$(11)$$

where C_g is the coefficient of compressibility; $k_{\rm fi}$ is the initial permeability of secondary fractures; V is the gas concentration; φ is the porosity; μ is the gas viscosity; Z refers to the Z-factor; x, y, z are the distances in the Cartesian coordinate system; p is the pressure; subscript sc refers to standard conditions. Substituting the definition of pseudo-pressure and modified permeability modulus in Eq. (A-5) and Eq. (A-6), the dimensionless continuity equation for secondary fractures can be given as

$$e^{-\alpha_{\rm D} m_{\rm D}} \left(\frac{\partial^2 m_{\rm D}}{\partial^2 r_{\rm D}} + \frac{1}{r_{\rm D}} \frac{\partial m_{\rm D}}{\partial r_{\rm D}} - \alpha_{\rm D} \left(\frac{\partial m_{\rm D}}{\partial r_{\rm D}} \right)^2 - \alpha_{\rm D} \left(\frac{\partial m_{\rm D}}{\partial z_{\rm D}} \right)^2 + \frac{\partial^2 m_{\rm D}}{\partial^2 z_{\rm D}} \right)$$

$$= \omega \frac{\partial m_{\rm D}}{\partial t_{\rm D}} + (1 - \omega) \frac{\partial V_{\rm D}}{\partial t_{\rm D}}$$
(12)

where ω is the storativity ratio. After dimensionless treatment, the initial conditions and boundary conditions can be written as

$$m_{\rm D}|_{t_{\rm D}=0}=0\tag{13}$$

$$\lim_{r_{\rm D}\to 0} e^{-\alpha_{\rm D} m_{\rm D}} \frac{\partial m_{\rm D}}{\partial r_{\rm D}} \bigg|_{r_{\rm D}} = -q_{\rm WD} \tag{14}$$

$$\lim_{r_{\rm D}\to\infty} m_{\rm D}|_{r_{\rm D}} = 0 \tag{15}$$

$$\left. \frac{\partial m_{\rm D}}{\partial z_{\rm D}} \right|_{z_{\rm D}=0} = \left. \frac{\partial m_{\rm D}}{\partial z_{\rm D}} \right|_{z_{\rm D}=h_{\rm D}} = 0 \tag{16}$$

where $h_{\rm D}$ is the dimensionless formation thickness. Combining the adsorption equation in Eq. (30), $V_{\rm D}$ in Eq. (29) can be further written as

$$s\overline{V}_{D} = 3aD_{D} \left[\sqrt{\frac{s}{D_{D}}} \coth\left(\sqrt{\frac{s}{D_{D}}}\right) - 1 \right] \overline{m}_{D}$$
 (17)

where s is the Laplace variable; D_D refers to the dimensionless diffusion coefficient; a is the adsorption index; V_D is the dimensionless gas concentration; \overline{W}_D is the dimensionless concentration; \overline{m}_D is the dimensionless pseudo-pressure; superscript – represents

$$\xi_{\text{FD}ij} - \xi_{\text{FwD}} = \frac{2\pi}{C_{\text{FD}i}} \left[\frac{\Delta r_{\text{D}i}}{8} q_{\text{FD}ij} + \sum_{k=1}^{j-1} q_{\text{FD}ij} \left(\frac{\Delta r_{\text{D}i}}{2} + r_{\text{D}ij} - k\Delta r_{\text{D}i} \right) - r_{\text{D}ij} \sum_{k=1}^{M} q_{\text{FD}ki} \right]$$
(10)

where *M* is the number of fracture segments on each primary fracture; *ii* refers to the serial number of the fracture segment.

the Laplace transformation. Substituting Eq. (17) into the continuity equation of secondary fractures and performing perturbation transformation, the continuity equation in Eq. (12) can be further written as

$$\frac{\mathrm{d}^2 \bar{\xi}_{\mathrm{D}}}{\mathrm{d}^2 r_{\mathrm{D}}} + \frac{1}{r_{\mathrm{D}}} \frac{\mathrm{d} \bar{\xi}_{\mathrm{D}}}{\mathrm{d} r_{\mathrm{D}}} = f(s) \bar{\xi}_{\mathrm{D}}$$
(18)

2.2.2. Secondary fracture system

The continuity equation of secondary fracture system is

where f(s) is given as

$$f(s) = \omega s + (1 - \omega) 3aD_{D} \left[\sqrt{s/D_{D}} \coth\left(\sqrt{s/D_{D}}\right) - 1 \right]$$
 (19)

The general solution can be expressed as

$$\overline{\xi}_{\rm D} = \overline{q}_{\rm D} K_0 \left[\sqrt{f(s)} \, r_{\rm D} \right] \tag{20}$$

with

$$r_{\rm D} = \sqrt{(x_{\rm D} - x_{\rm wD})^2 + (y_{\rm D} - y_{\rm wD})^2}$$
 (21)

$$a = \frac{3.684 \times 10^{-3} \mu Z p_{sc} q_{sc} T}{2k_{fi} h T_{sc}} \frac{V_{L} p_{L}}{(p_{L} + p)(p_{L} + p_{i})(p + p_{i})}$$
(22)

$$m_{\rm D} = -\frac{1}{\alpha_{\rm D}} \ln(1 - \alpha_{\rm D} \xi_{\rm D}) \tag{23}$$

where V_L and p_L are the Langmuir volume and pressure; $x_{\rm wD}$ and $y_{\rm wD}$ are the dimensionless origin coordinates; K_0 is the zero-order Bessel function of the second kind; T is the temperature.

2.2.3. Matrix system

The matrix system is composed of an infinite number of spherical units. The low permeability of shale reservoirs causes concentration differences rather than pressure differences to be the driving force. With Fick's diffusion law in Eq. (A-7) and the continuity equation in Eq. (A-8), the continuity equation of matrix is rearranged as

$$\frac{1}{r_{\rm m}^2} \frac{\partial}{\partial r_{\rm m}} \left(r_{\rm m}^2 D \frac{\partial V}{\partial r_{\rm m}} \right) = \frac{\partial V}{\partial t} \tag{24}$$

where $r_{\rm m}$ refers to the radial distance of the matrix system; subscript m denotes matrix system. The adsorption process on the surface of the matrix spherical unit is transient and satisfy Langmuir's adsorption law.

$$\frac{4\pi R_{\rm m}^3}{3} \frac{\partial V}{\partial t} = 4\pi R_{\rm m}^2 D \frac{\partial V}{\partial r_{\rm m}} \Big|_{r_{\rm m}=R_{\rm m}}$$
 (25)

where $R_{\rm m}$ is the radius of spherical matrix unit. The initial conditions of the spherical matrix unit can be expressed as

$$V|_{t=0} = V_{i} \tag{26}$$

The inner and outer boundary conditions are defined as

$$\lim_{r_{\rm m}\to 0} \frac{\partial V}{\partial r_{\rm m}} \bigg|_{r_{\rm m}} = 0 \tag{27}$$

$$V|_{r_{\rm m}=R_{\rm m}}=V_{\rm e}\tag{28}$$

where $V_{\rm e}$ refers to the gas concentration at the outer boundary of the matrix unit. After Laplace transformation, the dimensionless governing equation of matrix system is given as

$$\frac{1}{r_{\rm mD}^2} \frac{\rm d}{{\rm d}r_{\rm mD}} \left(r_{\rm mD}^2 \frac{{\rm d}\overline{V}_{\rm D}}{{\rm d}r_{\rm mD}} \right) = \frac{s\overline{V}_{\rm D}}{D_{\rm D}} \tag{29}$$

Meanwhile, the inner and outer boundary conditions of the matrix unit in Laplace domain are

$$s\overline{V}_{D} = 3D_{D} \frac{d\overline{V}_{D}}{dr_{mD}}\Big|_{r=r-1}$$
(30)

$$\lim_{r_{mD} \to 0} \frac{d\overline{V}_D}{dr_{mD}} \Big|_{r_{mD}} = 0 \tag{31}$$

$$\overline{V}_{D}|_{r_{mD}=1} = \overline{V}_{eD} \tag{32}$$

where V_{eD} is the dimensionless concentration at outer boundary. The general solution of the governing matrix equation is

$$\overline{V}_{D} = \frac{Ae^{-r_{mD}\sqrt{s/D_{D}}} + Be^{r_{mD}\sqrt{s/D_{D}}}}{r_{mD}}$$
(33)

The undetermined coefficients in the above general solution can be determined as

$$A = -\frac{a\overline{m}_{\rm mD}}{\sinh\left(\sqrt{s/D_{\rm D}}\right)}, \quad B = \frac{a\overline{m}_{\rm mD}}{\sinh\left(\sqrt{s/D_{\rm D}}\right)}$$
(34)

2.2.4. Boundary system

The meshless boundary element method is used to deal with the irregular outer boundaries of multi-well horizontal pads in shale gas reservoirs. In order to obtain the boundary integral equation, the general solution for differential equation in Eq. (11) should satisfy

$$\nabla^2 K_0 \left(\sqrt{f(s)} \, r_{\rm D} \right) - f(s) K_0 \left(\sqrt{f(s)} \, r_{\rm D} \right) + \delta(r_{\rm D}) = 0 \tag{35} \label{eq:35}$$

where ∇^2 is the Laplacian. Using the properties of the δ function, Eq. (35) can be further simplified to

$$\int_{\Omega} \left[\overline{\xi}_{D}(r_{D}) \nabla^{2} K_{0} \left(\sqrt{f(s)} r_{D} \right) - K_{0} \left(\sqrt{f(s)} r_{D} \right) \nabla^{2} \overline{\xi}_{D}(r_{D}) \right] d\Omega
+ \overline{\xi}_{D}(r_{D}) - \frac{1}{f(s)} \sum_{j=1}^{N} K_{0} \left(\sqrt{f(s)} r_{D,j} \right) q_{D,j}
= 0$$
(36)

where N is the total number of all fracture segments; Ω is the border-domain; $q_{\mathrm{D},\mathrm{J}}$ refers to the dimensionless flux rate term for each boundary segment. According to the Green's second formula, the final boundary integral equation can be given as

$$\overline{\xi}_{D}(r_{D}) = \int_{\Omega} \left[K_{0} \left(\sqrt{f(s)} \, r_{D} \right) \frac{\partial \overline{\xi}_{D}(r_{D})}{\partial n} - \overline{\xi}_{D}(r_{D}) \frac{\partial K_{0} \left(\sqrt{f(s)} \, r_{D} \right)}{\partial n} \right] d\Gamma
+ \frac{1}{f(s)} \sum_{j=1}^{N} K_{0} \left(\sqrt{f(s)} \, r_{D,j} \right) q_{D,j}$$
(37)

where n refers to the normal direction. As given in Fig. 1, for each linear segment of the irregular outer boundary, the boundary integral equation in Eq. (37) can be further expressed as

$$\theta_{k}\overline{\xi}_{D}(r_{D,k}) = \sum_{i=1}^{B} \int_{\Omega} \left[K_{0}\left(\sqrt{f(s)} \, r_{D,k}\right) \frac{\partial \overline{\xi}_{D}(r_{D})}{\partial n} - \overline{\xi}_{D}(r_{D}) \frac{\partial K_{0}\left(\sqrt{f(s)} \, r_{D,k}\right)}{\partial n} \right] d\Gamma + \frac{1}{f(s)} \sum_{j=1}^{N} K_{0}\left(\sqrt{f(s)} \, r_{D,j}\right) q_{D,j}$$

$$(38)$$

where B is the number of boundary segments and $k = 1, 2, 3, ..., N_b$. Introducing the linear element method to perform the difference on Eq. (38), one can get

superposition between the fracture nodes and boundary nodes, its reciprocity can be given as

$$\theta_{k}\overline{\xi}_{D}(r_{D,k}) = \sum_{i=1}^{B} \int_{\Omega} \left[K_{0}\left(\sqrt{f(s)} \, r_{D,k}\right) \frac{\partial \overline{\xi}_{D}(r_{D})}{\partial n} - \left(\phi_{1}\overline{\xi}_{D,i} + \phi_{2}\overline{\xi}_{D,i+1}\right) \frac{\partial K_{0}\left(\sqrt{f(s)} \, r_{D,k}\right)}{\partial n} \right] d\Gamma + \frac{1}{f(s)} \sum_{j=1}^{N} K_{0}\left(\sqrt{f(s)} \, r_{D,j}\right) q_{D,j}$$

$$(39)$$

where θ_k is the angle of integration. For the global coordinate system in Eq. (39), it needs to be replaced by the local coordinate system. The integral relationship between tiny elements in the two coordinate systems is given as

$$d\Gamma = \sqrt{dx^2 + dy^2} = \sqrt{\left(\frac{x_{i+1} - x_i}{2}\right) + \left(\frac{y_{i+1} - y_i}{2}\right)} d\xi = \frac{l_i}{2} d\xi \qquad (40)$$

where l_i is the length of i-th integration segment. Therefore, the integral equation on each impermeable boundary segment is

$$\overline{\xi}_{D} \Big[r_{D,i,j} \Big(x_{D,B}, y_{D,B}; x_{wD}, y_{wD} \Big) \Big] \Big|_{\Pi} = \sum_{i=1}^{B} \overline{\xi}_{D,i} (r_{D,i}) \Big|_{\Omega}$$
 (45)

The reciprocity between various boundary nodes of the outer boundary can be written as

$$\overline{\xi}_{\mathrm{D}}\left[r_{\mathrm{D};i,j}\left(x_{\mathrm{D},\mathrm{B}},y_{\mathrm{D},\mathrm{B}};x_{\mathrm{w}\mathrm{D}},y_{\mathrm{w}\mathrm{D}}\right)\right]\Big|_{\Omega} = \sum_{i=1}^{B} \overline{\xi}_{\mathrm{D};i}\left(r_{\mathrm{D};i}\right)\Big|_{\Omega}$$
(46)

For the target well and adjacent wells, its flow constraints dur-

$$\theta_{k}\overline{\xi}_{\mathrm{D}}(r_{\mathrm{D},k}) = \sum_{i=1}^{B} \frac{l_{i}}{2} \int_{-1}^{1} \left[K_{0}\left(\sqrt{f(s)} \, r_{\mathrm{D},k}\right) \frac{\partial \overline{\xi}_{\mathrm{D}}(r_{\mathrm{D}})}{\partial n} - \left(\phi_{1}\overline{\xi}_{\mathrm{D},i} + \phi_{2}\overline{\xi}_{\mathrm{D},i+1}\right) \frac{\partial K_{0}\left(\sqrt{f(s)} \, r_{\mathrm{D},k}\right)}{\partial n} \right] \mathrm{d}\xi + \frac{1}{f(s)} \sum_{j=1}^{N} K_{0}\left(\sqrt{f(s)} \, r_{\mathrm{D},j}\right) q_{\mathrm{D},j}$$

$$\tag{41}$$

2.2.5. Solution procedure

The dimensionless position can be given as

$$r_{D;i,j}(x_{D},y_{D};x_{wD},y_{wD}) = \sqrt{\left(x_{D;i,j} - x_{wD}\right)^{2} + \left(y_{D;i,j} - y_{wD}\right)^{2}}$$
(42)

Combining with the boundary element method, the coordinates of the i-th segment nodes for j-th fracture in Fig. 1 can be expressed as

$$\begin{cases} x_{D;i,j} = x_{D;i} - l_{D:j} \cos \beta_i \\ y_{D;i,j} = y_{D;i} - l_{D:j} \cos \beta_i \end{cases}$$
(43)

where β is the fracture angle. The pressure superposition between various fracture segments in a multi-well horizontal pad is shown as

$$\overline{\xi}_{D}[r_{D;i,j}(x_{D},y_{D};x_{WD},y_{WD})]\big|_{\Pi} = \sum_{i=1}^{N_{F}} \sum_{i=1}^{M_{j}} \overline{\xi}_{D;i,j}(r_{D;i,j})\big|_{\Pi}$$
(44)

where N_F refers to the number of primary fractures; M is the number of nodes on each primary fracture. For the pressure

ing constant production rate can be expressed as

$$\sum_{j=1}^{1} \sum_{i=1}^{M_{j}} \left[\frac{\overline{q}_{i,j}(r_{D;i,j})|_{\Pi}}{\overline{q}_{sc}} \times \frac{l_{i}}{L} \right] = \frac{1}{s}$$
 (47)

$$\sum_{j=2}^{N_{w}} \sum_{i=1}^{M_{j}} \left[\frac{\overline{q}_{i,j}(r_{D;i,j})}{\overline{q}_{sc}} \times \frac{l_{i}}{L} \right] = \frac{n}{s}$$

$$(48)$$

where L is the reference length; and $N_{\rm w}$ is the number of wells. In summary, the total equations in Eq. (49) include a number N of Eq. (20) (for secondary fractures), a number N of Eq. (10) (for primary fractures), a number B of Eq. (41) (for boundary nodes), Eq. (48) with quantity $N_{\rm w}-1$, and Eq. (47) with quantity 1. The unknown variables in Fig. 2 include the flow rate and pressure terms for the fracture segments and boundary nodes, as well as the bottom-hole pressure term. Since the outer boundary is impermeable, its flow rate term can be ignored. The total number of unknowns is $2N + B + N_{\rm w}$. The coefficient matrix, composed of the governing equations and unknown variables, is shown in Eq. (49).

H.-Y. Chu, S.-D. Fang, Z.-Q. Ren et al. Petroleum Science 22 (2025) 1155-1170

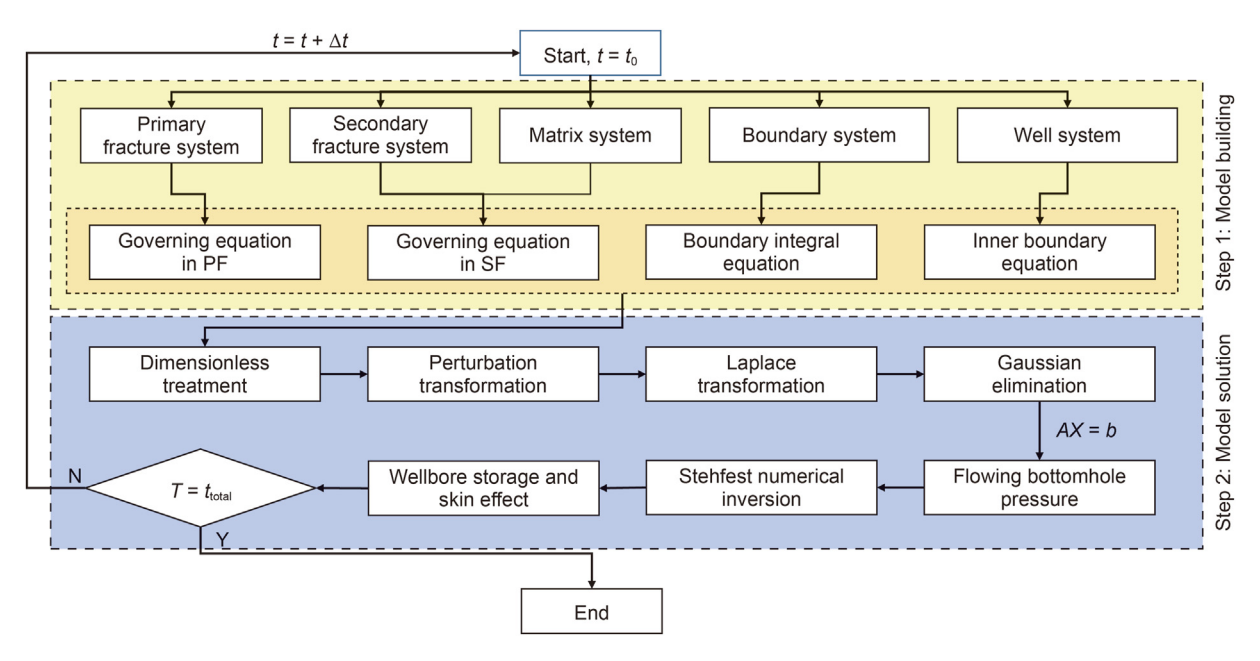


Fig. 2. The flow chart of the integrated multi-scale approach for multi-well horizontal pads in shale gas reservoirs.

$$\begin{bmatrix} \boldsymbol{A}_{1,N\times N} & \boldsymbol{A}_{2,N\times N} & \boldsymbol{E}_{N\times B} \\ \boldsymbol{B}_{1,N\times N} & \boldsymbol{B}_{2,N\times N} & \boldsymbol{0}_{N\times B} \\ \boldsymbol{F}_{1,B\times N} & \boldsymbol{F}_{2,B\times N} & \boldsymbol{F}_{B\times B} \\ \boldsymbol{C}_{N_{w}\times N} & \boldsymbol{0} & \boldsymbol{0} \end{bmatrix} \times \begin{bmatrix} \overline{\boldsymbol{q}}_{D,N\times 1} \\ \overline{\boldsymbol{\xi}}_{D,(N+B)\times 1} \\ \overline{\boldsymbol{\xi}}_{wD,N_{w}\times 1} \end{bmatrix} = \begin{bmatrix} \boldsymbol{0}_{2N+B} \\ 1/s \\ (\boldsymbol{n/s})_{(N_{w}-1)\times 1} \end{bmatrix}$$

$$(49)$$

The influence of wellbore storage coefficient and skin factor on bottom hole pressure can be given as

$$\overline{\xi}_{\text{WD}}(u, S, C_{\text{D}}) = \frac{S + u\overline{\xi}_{\text{WD}}}{S + C_{\text{D}}u^2(u\overline{\xi}_{\text{WD}} + S)}$$
(50)

where C_D is the wellbore storage coefficient; S is the skin factor. The Stehfest numerical inversion method in Eq. (51) is used to transform the pressure solution in Laplace domain (Stehfest, 1970).

$$\xi_{\text{WD}} = \frac{\ln 2}{t} \sum_{i=1}^{N} V_i \overline{\xi}_{\text{WD}}(s)$$
 (51)

where N is an empirical constant and the definition of V_i can be expressed as

Table 1The input parameters for the numerical simulator validation.

Group	Item	Value	Unit
Shale formation	Initial pressure	34.47	MPa
	Reservoir thickness	9.14	m
	Porosity	0.1	_
	Rock compressibility	4.35×10^{-4}	MPa^{-1}
	Permeability	0.1	mD
	Well spacing	250	m
Primary fractures	PF width	1.0×10^{-3}	m
	PF number for testing well	4	_
	PF number for adjacent well	4	_
	PF conductivity for testing well	450	mD m
	PF conductivity for adjacent well	450	mD m
	PF half-length for testing well	30	m
	PF half-length for adjacent well	50	m
	PF dip angle	90	0
MFHWs	Well length for testing well	750	m
	Well length for adjacent well	750	m
	Well radius	9.14×10^{-2}	m
	Production rate	1	m³/d
	Skin factor	0	_
	Wellbore storage coefficient	0.23	m³/MPa

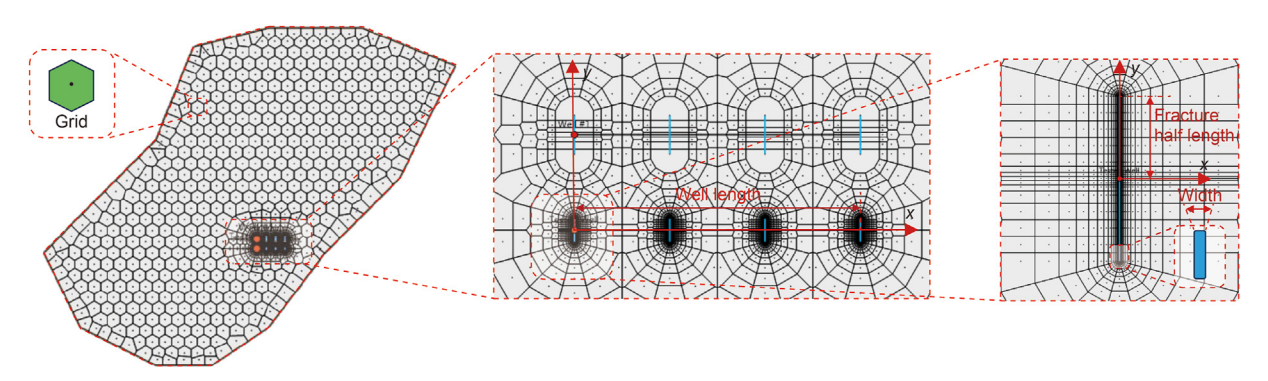


Fig. 3. The mesh generation results for the multi-well horizontal pad in shale gas reservoirs.

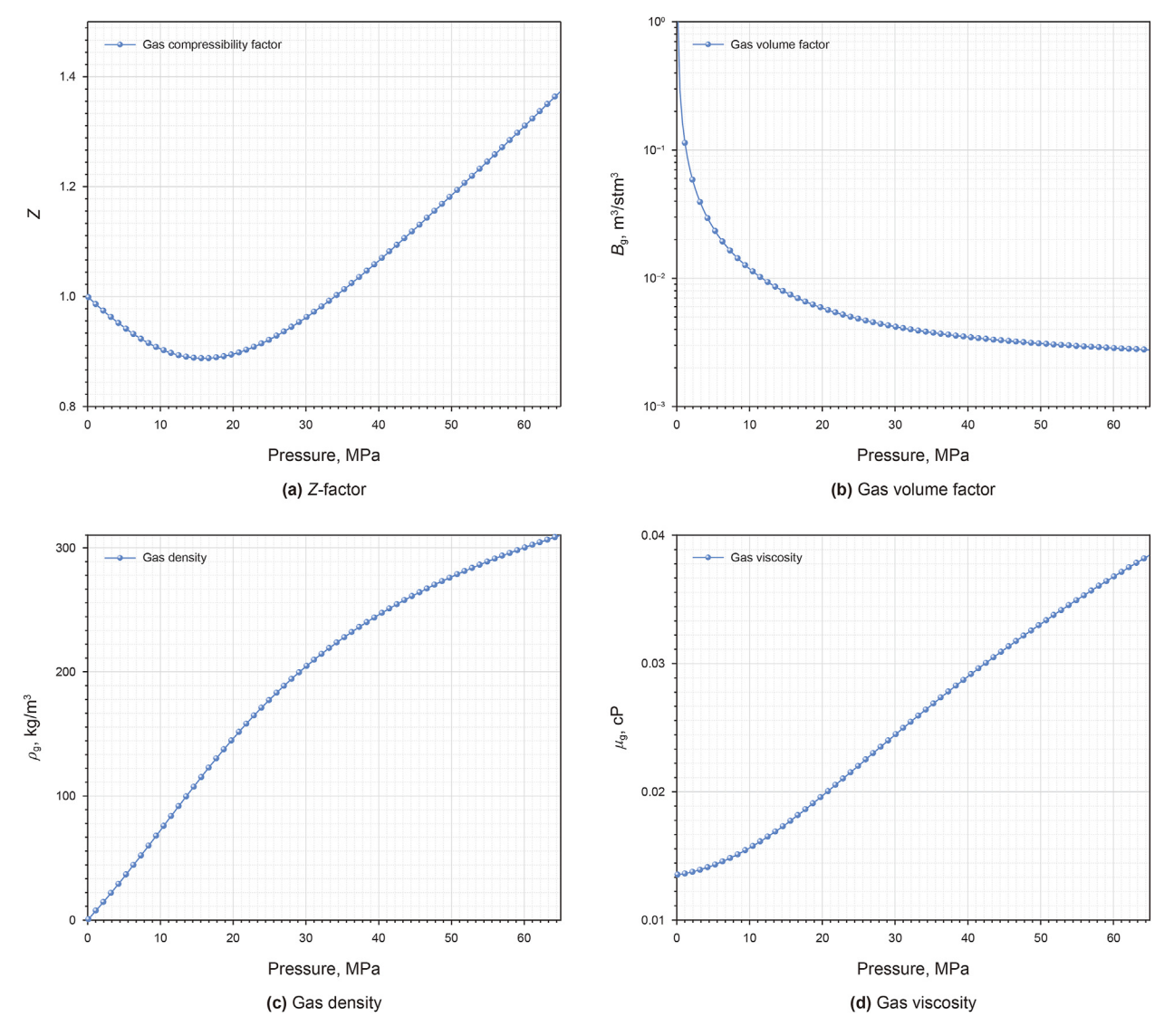


Fig. 4. The physical properties of shale gas used in the methodology verification.

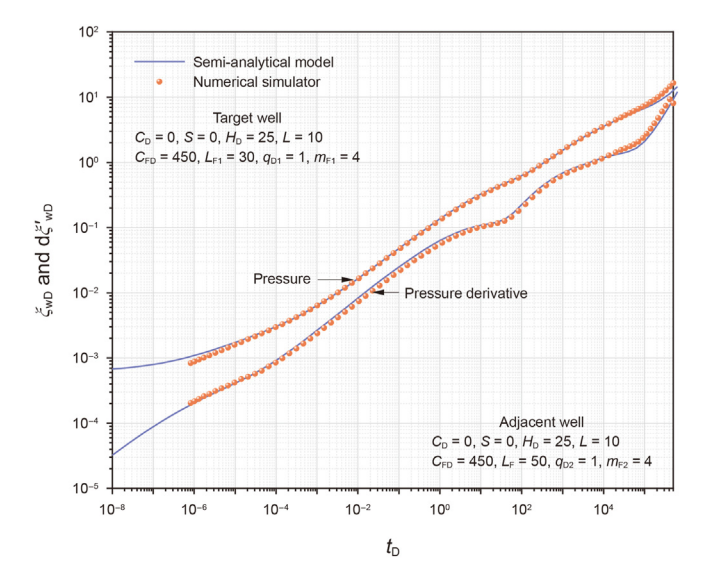


Fig. 5. The comparison of calculation results between the commercial numerical simulator and the proposed multi-scale method.

$$V_{i} = (-1)^{N/2+i} \sum_{k=(i+1)/2}^{\min(i,N/2)} \frac{k^{N/2+1}(2k)!}{(N/2-k)!k!(k-1)!(i-k)!(2k-i)!}$$
(52)

2.3. Methodology verification

To verify the proposed method, a commercial numerical simulator (KAPPA) is employed in this study due to the lack of available actual data. The numerical model, as illustrated in Fig. 3, features an irregular impermeable boundary. The verification process focuses on two fractured horizontal wells operating under constant production rate conditions. Both wells have a length of 750 m, and four hydraulic fractures with a conductivity of 450 mD m are evenly distributed at the root end and toe section of each well. The well spacing within the well pad is set at 250 m. For simplicity, it is assumed that primary fractures within the same well share the same properties, such as fracture angle, length, and conductivity. Additional details regarding the reservoirs, wells, and fractures can

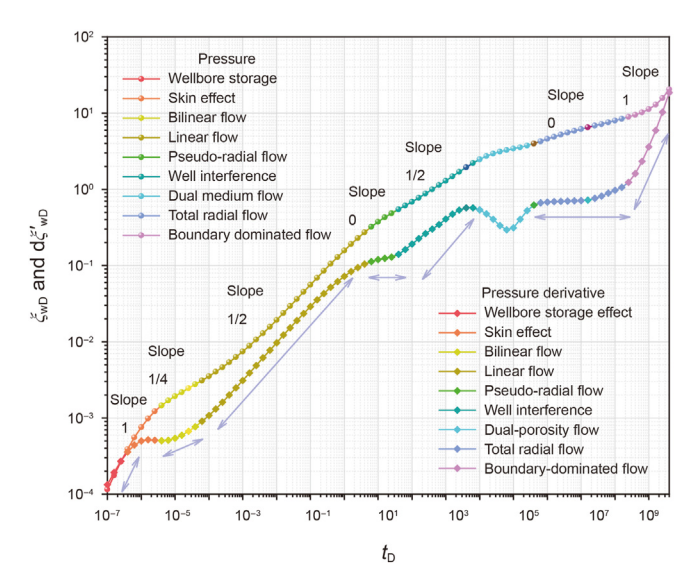


Fig. 6. The typical pressure transient behavior of multi-well horizontal pads with well interference in shale gas reservoirs.

be found in Table 1. The physical properties of shale gas, including gas compressibility coefficient, density, viscosity, and Z-factor, are presented in Fig. 4. The numerical simulator employs grid refinement techniques to describe the multi-scale multi-well horizontal pad in shale gas reservoirs. The finite volume method is utilized to solve the equation group constructed using irregular PEBI grids. Fig. 5 demonstrates that the proposed method exhibits a small error compared to the numerical simulation method, thereby ensuring its reliability. This small error stems from the fundamental differences between the two methods in how they handle inner boundaries. The proposed method typically employs boundary integral equations to address boundary conditions, while traditional numerical methods generally approximate or interpolate boundary conditions on the discretized grid. By eliminating the need for grid discretization across the entire study area, the smaller-dimensional coefficient matrix offers a significant improvement in computational performance for the proposed model. However, the incorporation of the analytical source function restricts the proposed method to the domain of single-phase flow.

3. Results and discussion

3.1. Comparison of typical pressure behavior

The pressure and its derivative in Fig. 6 serve as diagnostic tools for identifying the various flow regimes present in multi-well horizontal pads within shale gas reservoirs. To enhance clarity and distinguish between different periods of flow, an optimal combination of parameters for the multi-well horizontal pad was determined. By analyzing the logarithmic diagnostic plot of the pressure derivative curve, typical pressure behavior can be classified into several distinct flow regimes: wellbore storage effect, skin effect, bilinear flow, linear flow, pseudo-radial flow of primary fractures, well interference period, dual-porosity flow, pseudoradial flow of the total system, boundary-dominated flow. Initially, the shale gas molecules are adsorbed within the reservoir without diffusion and desorption. The flow regimes identified by the pressure derivative curve exhibit similarities to those observed in conventional gas reservoirs, where the driving force is the concentration difference of shale gas molecules. Therefore, the presence of bilinear flow, linear flow, dual-porosity flow, and pseudoradial flow reflects the multi-scale characteristics inherent in shale gas reservoirs.

The derivative curve during the wellbore storage stage displays a linear relationship with a slope of one. The presence of the skin effect within the reservoir induces an abnormal hump in the pressure derivative curve. Bilinear flow and linear flow are characterized by pressure derivative curves with slopes of 1/2 and 1/4. respectively. As the drainage area expands, the pseudo-radial flow of primary fractures becomes evident. Following the pseudo-radial flow of primary fractures, the reservoir's influence gradually becomes apparent. This influence stems from two sources. Firstly, it arises from the flow resulting from the diffusion and desorption of shale gas molecules. Secondly, it is driven by geological structures such as well interference and secondary fractures within the reservoir. Adsorbed shale gas molecules in the matrix are transported to secondary fractures through desorption and diffusion, resulting in the appearance of a V-shaped dip in the pressure derivative curve. During the pseudo-radial flow of the total system, multiple wells interact with each other to form a cohesive system. When the pressure response ultimately reaches the boundary, the pressure and its derivative exhibit a linear relationship with a slope of one. It is crucial to emphasize that linear flow with a slope of 1/2 manifests in two distinct phases. The initial phase of linear flow pertains to the migration of shale gas molecules in a linear manner towards the primary fractures. In contrast, the subsequent phase of linear flow is predominantly governed by well interference, wherein the shale gas molecules move towards the target well following a linear trajectory. This type of linear flow is most likely to occur under conditions where adjacent wells possess similar properties to the target well and the well spacing is sufficiently large. Under such circumstances, the multiple wells on a multi-well pad effectively function as distinct fractures within a single well system.

3.2. Sensitivity analysis

3.2.1. Effect of diffusion coefficient

The impact of diffusion coefficients on the pressure behavior of a multi-well horizontal pad is depicted in Fig. 7. The dimensionless diffusion coefficient is increased from 0.1×10^{-5} to 1×10^{-5} . Altering the diffusion coefficient influences the pressure derivative

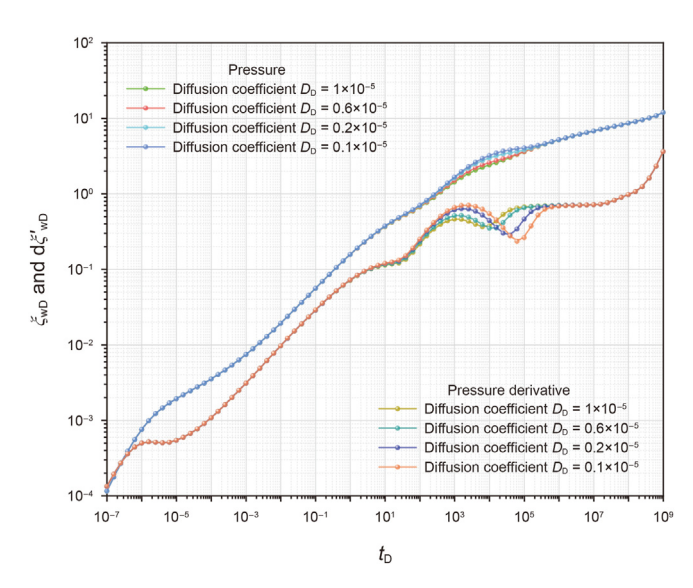


Fig. 7. Influence of diffusion coefficient on pressure behavior from multi-well horizontal pads with well interference in shale gas reservoirs.

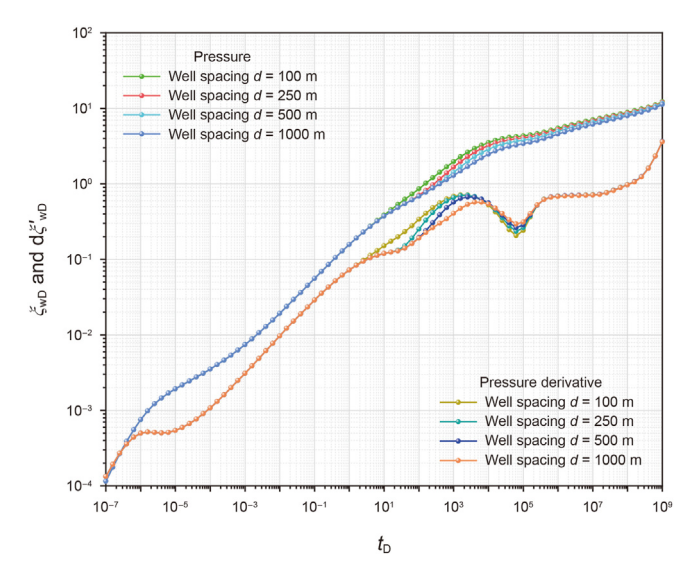


Fig. 8. Influence of well spacing on pressure behavior from multi-well horizontal pads with well interference in shale gas reservoirs.

behavior as indicated by the dual-porosity flow. As the diffusion coefficient increases, the V-shaped dip in the pressure derivative curve appears earlier. Conversely, the final value in the pressure curve is inversely proportional to the diffusion coefficient. Moreover, the amplitude and duration of the V-shaped dip exhibit an inverse relationship with the diffusion coefficient. This is because the diffusion coefficient determines the rate at which adsorbed shale gas molecules are transported from the matrix to the secondary fractures. This transportation process manifests as a Vshaped dip in the derivative curve. When the diffusion rate of shale gas molecules is rapid, the occurrence of this transportation between the two systems happens earlier. A higher diffusion rate also leads to a shorter duration of transportation between the two systems. The role of the diffusion coefficient in shale gas reservoirs resembles that of the interporosity flow coefficient in gas reservoirs.

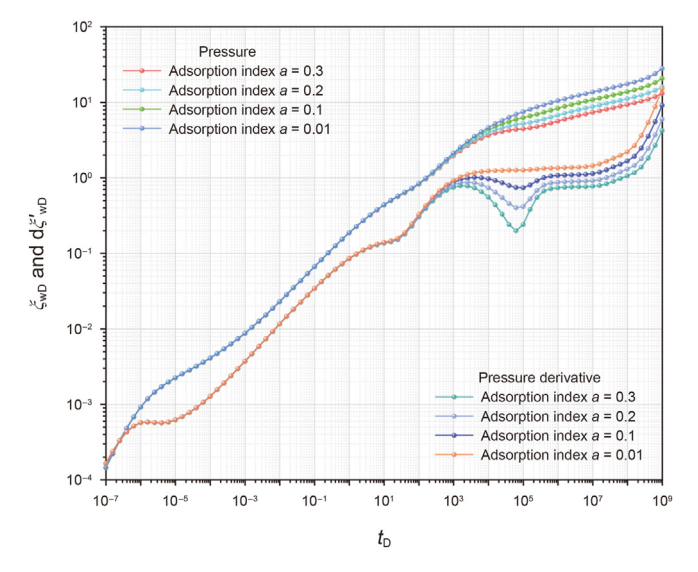


Fig. 9. Influence of adsorption index on pressure behavior from multi-well horizontal pads with well interference in shale gas reservoirs.

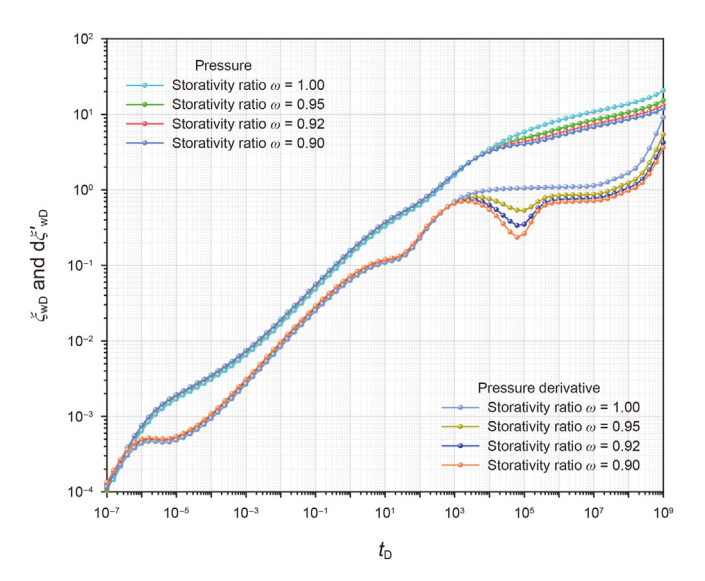


Fig. 10. Influence of storativity ratio on pressure behavior from multi-well horizontal pads with well interference in shale gas reservoirs.

3.2.2. Effect of well spacing

The effects of well spacing on the pressure behavior of a multiwell horizontal pad are presented in Fig. 8. The range of well spacing varies from 100 to 1000 m. It can be concluded that changes in well spacing have an impact on both well interference flow and the pseudo-radial flow of primary fractures. During these two stages, there exists an inverse relationship between well spacing and pressure derivative behavior. As the well spacing increases, the pseudo-radial flow of primary fractures becomes more prominent. Consequently, the start-stop time of transitional flow is postponed accordingly. During the transitional flow, the value of well spacing also determines the slope of the derivative curve. When the well spacing is appropriately chosen, two adjacent fractured horizontal wells can be approximated as two primary fractures. At this point, the transitional flow exhibits the characteristics of linear flow. When the well spacing increases to 1000 m, the impact of well interference becomes negligible, and the derivative curve during the transitional period shows an elliptical flow with a slope of 1/3.

3.2.3. Effect of adsorption index

The impact of the adsorption index on transient pressure behavior is illustrated in Fig. 9. The adsorption index plays a crucial role in shaping the pressure response during the V-shaped dip, pseudo-radial flow of the entire system, and boundary-dominated flow. Analyzing the pressure curve, we observe an inverse correlation between the pressure values at these three flow stages and the adsorption index. As the adsorption index increases, the V-shaped dip in the pressure derivative becomes more pronounced. This can be attributed to the fact that the adsorption index determines the quantity of natural gas present in the adsorbed state within the matrix system. A higher adsorption index implies a greater flow rate of adsorbed natural gas from the matrix system into the secondary fracture system. Regarding the pseudo-radial flow of the overall system, the adsorption index exhibits an inverse relationship with the value of the derivative curve.

3.2.4. Effect of storativity ratio

Fig. 10 illustrates the impact of storativity ratio on pressure behavior in a multi-well horizontal pad with well interference. The storativity ratio ranges from 0.90 to 1. Changes in the storativity

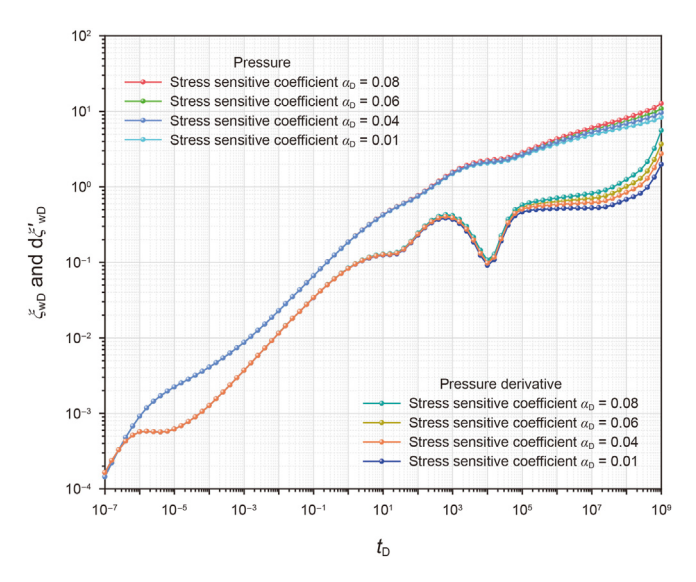


Fig. 11. Influence of stress sensitive coefficient on pressure behavior from multi-well horizontal pads with well interference in shale gas reservoirs.

ratio influence the pressure behavior during the V-shaped dip, the pseudo-radial flow of the entire system, and the boundary-dominated flow. Specifically, the storativity ratio directly affects the pressure values in these three stages. In terms of the pressure derivative, an increase in the storativity ratio enhances the prominence of the V-shaped dip. There exists an inverse relationship between the amplitude of the V-shaped dip and the storativity ratio. This can be attributed to the fact that a higher storativity ratio increases the dependence of fluid flow on the secondary fracture system with greater permeability. Furthermore, for both the pseudo-radial flow of the entire system and the boundary-dominated flow, the value of pressure derivative is directly proportional to the storativity ratio.

3.2.5. Effect of stress sensitive coefficient

Fig. 11 demonstrates the impact of the stress sensitive coefficient on transient pressure behavior. The stress sensitive coefficient ranges from 0.01 to 0.08. It is evident that changes in the stress sensitive coefficient influence the pressure behavior during the pseudo-radial flow of the total system and the boundary-dominated flow. Specifically, the pressure behavior during these two flow stages is directly proportional to the stress sensitive coefficient. This relationship can be attributed to the more pronounced stress sensitivity observed in shale gas reservoirs with lower permeability. Consequently, the flow of shale gas in these reservoirs experiences greater hindrance. As the stress sensitive coefficient increases, the slope of the derivative curve during the pseudo-radial flow of the total system decreases, leading to a delay in the occurrence of the boundary-dominated flow.

3.3. Case study

3.3.1. Geologic overview

In Fig. 12, the Fuling area is situated in the southern part of the fold stratigraphic belt in the eastern Sichuan Basin and is influenced by the Shizhu syncline, the south side of the Wanxian syncline, and the Fangdoushan anticline (Guo et al., 2023). The edge zone of the Fuling area contains widely distributed fractures, while the main area has relatively rare fractures. The mineral composition in the area includes clay minerals, siliceous minerals, carbonate minerals, feldspar, and pyrite (Gou et al., 2020). Lithologically, it comprises

carbonaceous shale, silty shale, and black siliceous shale. The Wufeng Formation and Longmaxi Formation are the primary gasbearing formations in the area, formed in the Late Ordovician and Early Silurian, respectively. As of 2022, the proven reserves of shale gas reservoirs in the Fuling area are $8975\times10^8\ m^3.$

Focusing on the Jiaoshiba Block in the eastern section of the Fuling area, it is located approximately 100 km northeast of Chongqing city and has a gas-bearing area of 383.54 km², with a burial depth range of 2300–3500 m. The Wufeng Formation and Longmaxi Formation in this block have a total thickness of 89 m, with the main gas-producing layer measuring 38 m (Pang et al., 2015). The proven reserves in the Jiaoshiba Block reach 3805.98×10^8 m³ (Guo, 2019), and the initial pressure range falls within 36-40 MPa. The matrix permeability and porosity of this block are 1.3×10^{-3} mD and 4%, respectively (Pang et al., 2015). Table 2 gives the further detailed properties of the Jiaoshiba Block.

3.3.2. Recovery history

The recovery history of the Fuling shale gas reservoir can be divided into three distinct periods (Guo et al., 2023). The first period, spanning from 2009 to 2012, is referred to as the exploration stage. During this stage, the exploratory well JY1HF achieved a significant recovery rate, reaching 20.3 \times 10⁴ m³/d in November 2012. The second stage marks the pilot production stage, which took place from 2012 to 2017. In this period, three new exploration wells, namely JY2, JY3, and JY4, were deployed in the Jiaoshiba anticline to explore the expansive 594.5 km² area of the Fuling shale gas reservoir. Additionally, the IY1HF well began its transition to the pilot production stage, demonstrating an average gas productivity of 5.0×10^8 m³/a. Furthermore, four exploratory wells were utilized to investigate the complex structural area encompassing an additional 550 km² on the periphery of the Jiaoshiba anticline. Among these wells, JY8 showcased a remarkable gas production rate of 20.9×10^4 m³/d. The cumulative production volume of the Fuling shale gas field exceeded $100 \times 10^8 \text{ m}^3$ throughout this second stage. The third phase commenced in 2018, during which a total of 244 infill wells were drilled in the Jiaoshiba block. As of 2022, the number of production wells drilled in the Fuling shale gas reservoir had reached 650. Notably, nearly all of these wells are multiple fractured horizontal wells. The cumulative gas production volume of the Fuling shale gas reservoir currently stands at 416.6 \times 10⁸ m³.

3.3.3. Rate transient analysis

Fig. 13 displays the collection of wellhead pressure behavior and daily production rate behavior of the target well, which were observed over a time span of up to 6000 h. The data was gathered under varying flow pressure and rate conditions. After roughly 2000 h, both the daily gas production and wellhead pressure curves showed a sharp downward trend, which persisted for 2400 h. Notably, the recovery in wellhead pressure data began at 2830 h, which coincided with the adjacent well undergoing fracturing treatments. This provides evidence of well interference between the two wells. To process the wellhead pressure and gas production data, we utilized the rate-normalized pressure (RNP) and material balance time method, as detailed in Eqs. (53)–(55). The RTA analysis method, which is essentially a deconvolution method, was employed to obtain the pressure behavior at unit flow rate. As depicted in Fig. 14, the RNP and its derivative curves demonstrate that the flow regimes from Fuling shale gas reservoir include linear flow, transitional flow, and boundary-dominated flow. By employing the collected input parameters presented in Table 3, our proposed model underwent typical curve matching. The results of the typical curve matching indicate that the formation permeability is 2.58×10^{-2} mD, the well spacing is 227.8 m, the diffusion

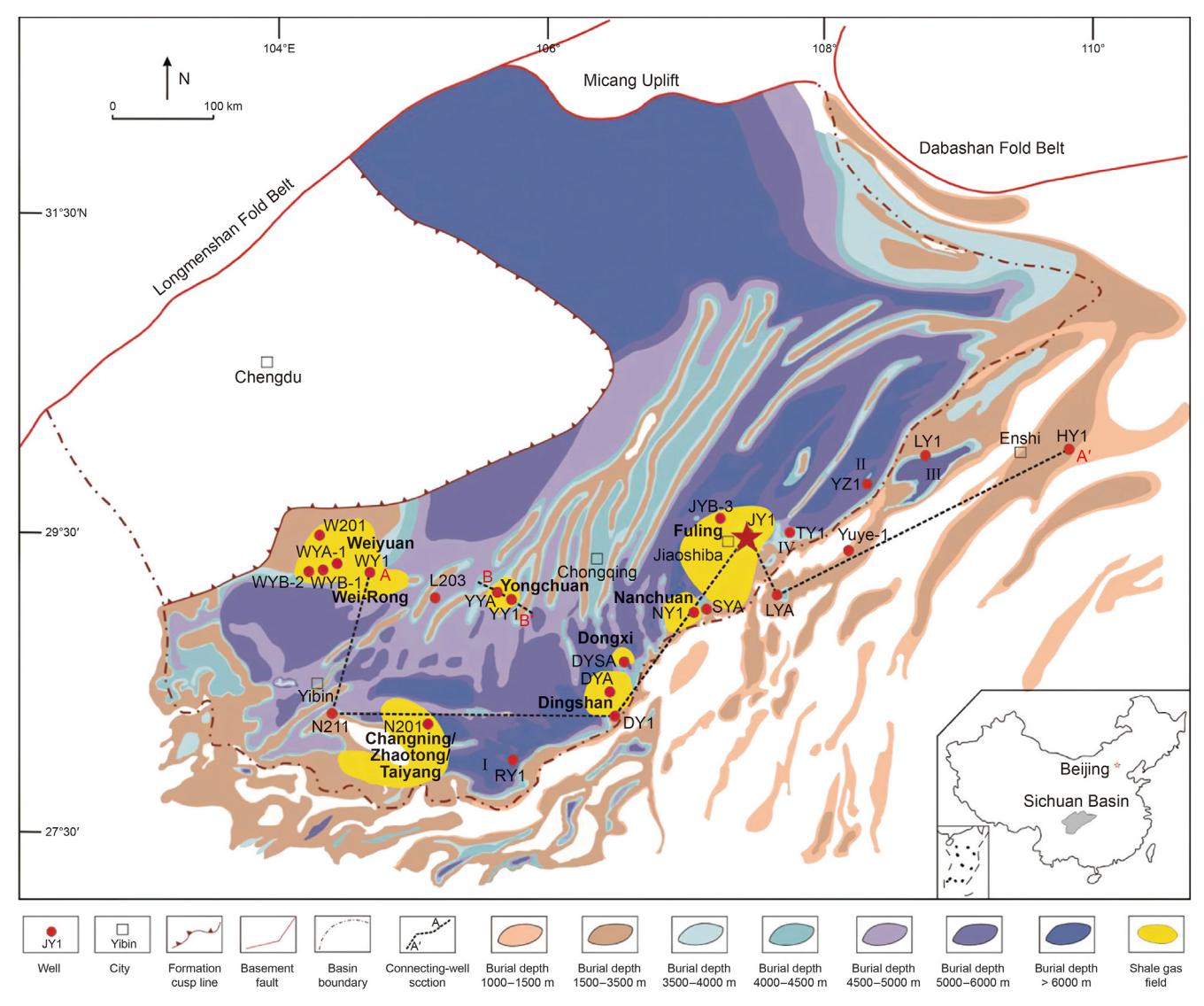


Fig. 12. The regional location and typical well location in the Fuling shale gas reservoir of the Sichuan Basin. The red star represents the typical well (modified from Nie et al., 2023).

Table 2
The detailed geological properties of the Jiaoshiba block in the Fuling shale gas reservoir (modified from Pang et al., 2015; Guo, 2019; Nie et al., 2020, 2023).

Item	Name/Value	Unit
Structural location	The eastern part of the Sichuan Basin and Jiaoshiba area	_
Lithology	Carbonaceous and silty shales and black siliceous shales	_
Sedimentary face	Deepwater shelf	_
Length of horizontal section	1000-1500	m
Depth	Over 2500	m
Matrix permeability	1.3×10^{-3}	mD
TOC	0.55-5.89	%
Target formation thickness	83-100	m
Shale gas reservoir thickness in high quality	38	m
Average porosity	4	%
Formation temperature	85	°C
Formation pressure	36-40	MPa
Average total gas content	4.3	m ³ /t
Kerogen type	I, II ₁	_ '

coefficient is 1.49×10^{-4} , and the skin factor is 0.09. Other parameters obtained are given in Table 4. The satisfactory fitting results obtained from the RNP curve represent only one of many

possible outcomes. To address the non-uniqueness in case study results, the results derived from wellhead pressure and gas production data across different wells and time periods should be

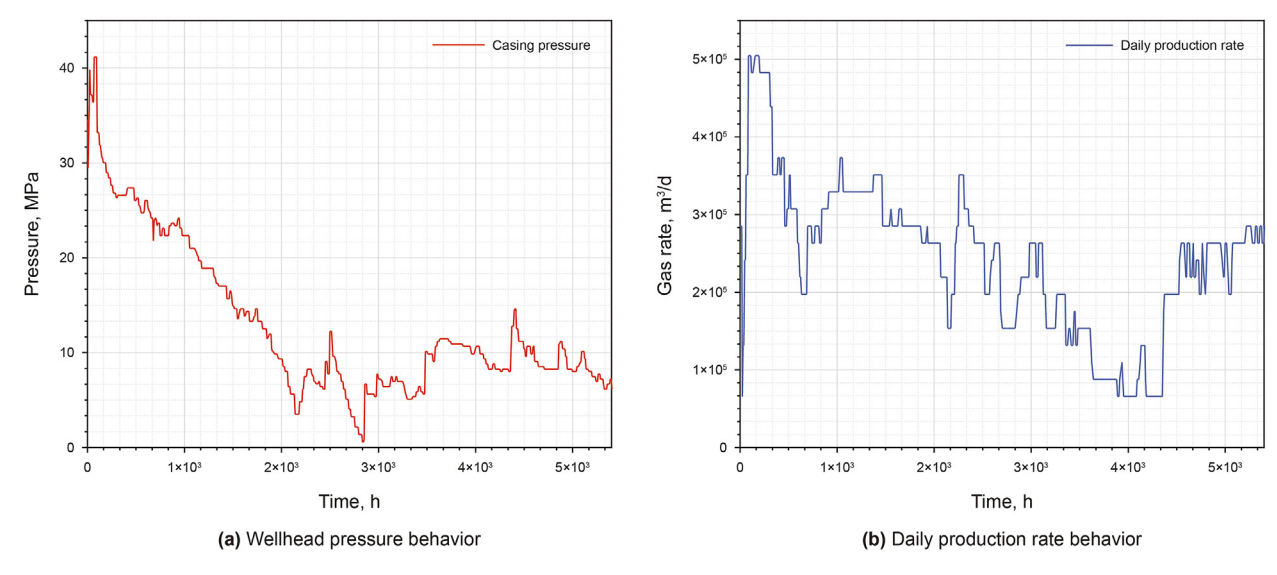


Fig. 13. The wellhead pressure and daily production rate behavior for typical well from the Fuling shale gas reservoir of the Sichuan Basin.

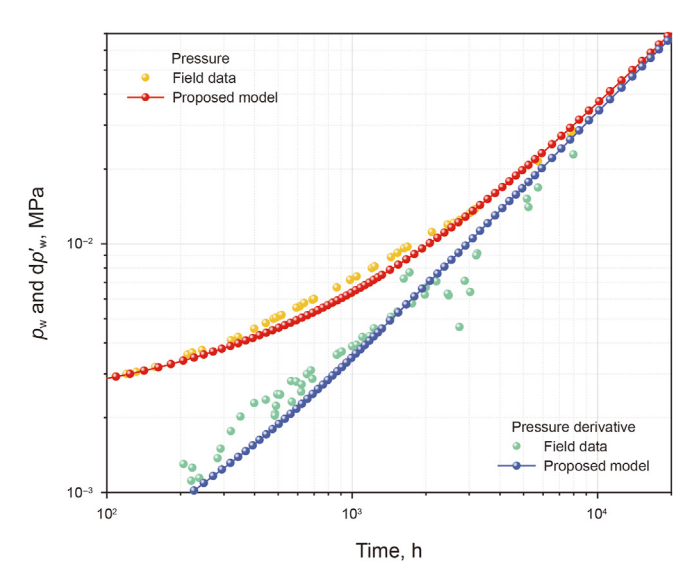


Fig. 14. The rate normalized pressure curve matching results of the proposed model and field data for the target well from the Fuling shale gas reservoir in the Sichuan Rasin

Table 3The input parameters of typical curves matching between the proposed model and actual data.

Group	Item	Value	Unit
Shale formation	Initial pressure	41.15	MPa
	Reservoir thickness	38	m
	Porosity	0.04	_
	Rock compressibility	4.35×10^{-4}	MPa^{-1}
Primary fractures	PF width	0.01	m
	PF number for testing well	55	_
	PF number for adjacent well	25	_
MFHWs	Well length for testing well	1009	m
	Well length for adjacent well	1304	m
	Well radius	0.09	m

compared with the current findings. Furthermore, additional monitoring techniques, such as fiber optic sensing and microseismic technology, should be employed to further mitigate the

Table 4The obtained parameters from typical curves matching

The obtained parameters from typical curves matching.				
Group	Item	Value	Unit	
Shale formation	Permeability	2.58×10^{-2}	mD	
	Well spacing	227.8	m	
	Diffusion coefficient	1.49×10^{-4}	_	
	Omega	0.2	_	
Primary fractures	PF conductivity for testing well	1520.4	mD m	
	PF conductivity for adjacent well	1021	mD m	
	PF half-length for testing well	38	m	
	PF half-length for adjacent well	91	m	
	PF dip angle	90	0	
MFHWs	Skin factor	0.09	_	
	Wellbore storage coefficient	$1.5 imes 10^{-2}$	m³/MPa	

non-uniqueness of the results.

$$RNP = \frac{p_i - \xi_w}{q} \tag{53}$$

$$RNP' = \frac{dRNP}{dlnt_e}$$
 (54)

where q is the daily production rate; t_e is the material balance time.

$$t_{\rm e} = \frac{N_{\rm q}}{a} \tag{55}$$

where N_q is the cumulative production volume.

4. Conclusions

This paper proposes a multi-scale approach for transient analysis of multi-well horizontal pads with well interference in shale gas reservoirs. Model development and validation are carried out, and typical pressure behaviors are diagnosed using pressure derivatives. Sensitivity analysis is conducted to illustrate the model's robustness. Real data from a typical shale gas well in Fuling shale gas reservoir are used, in combination with rate transient analysis, to demonstrate the practicality of the model. The main conclusions are as follows.

- (1) Analysis of flow regimes shows that the complete flow regimes for multi-well horizontal pads in shale gas reservoirs include wellbore storage effect, skin effect, bilinear flow, linear flow, pseudo-radial flow of primary fractures, well interference stage, dual-porosity flow, pseudo-radial flow of the total system, and boundary-dominated flow. The diffusion coefficient in shale gas reservoirs plays a role similar to that of the interporosity flow coefficient in conventional gas reservoirs. Changes in well spacing can cause transitional flow, caused by interference, to exhibit linear flow characteristics. The adsorption index and storativity ratio jointly determine the amount of natural gas in the adsorbed state in the matrix system. The stress sensitivity coefficient makes it easier to observe boundary-dominated flow.
- (2) Well interference events have occurred in hundreds of wells in the Sichuan Basin. The typical well is best known in the Fuling shale gas reservoir due to its the longest production history. The typical RNP curve shows that this well can exhibit linear flow, transitional flow, and boundary-dominated flow. The obtained formation permeability and well spacing are 2.58×10^{-2} mD and 227.8 m. The diffusion coefficient and the skin factor are 1.49×10^{-4} and 0.09. Secondary fractures are considered to be the primary pathways for fluid migration during well interference events.

The limitations of the model primarily stem from the inherent non-uniqueness of the curve-fitting inversion results, as well as the neglect of dynamic fracture evolution effects. Future research should focus on incorporating a broader array of reservoir characterization techniques to mitigate the non-uniqueness of the inversion outcomes. Additionally, the dynamic evolution of fracture morphology should be integrated into the model to enhance its accuracy and predictive capability.

CRediT authorship contribution statement

Hong-Yang Chu: Conceptualization. **Si-Dong Fang:** Validation. **Zhi-Qiang Ren:** Methodology. **Jian-Dong Zou:** Supervision. **Ran Bi:** Validation. **Wei-Yao Zhu:** Writing — review & editing. **W. John Lee:** Supervision.

Declaration of competing interest

The authors declare that they have no known competing financial interests or personal relationships that could have appeared to influence the work reported in this paper.

Acknowledgement

We are very grateful to all the people who have contributed to this work. This work received funding support from the National Natural Science Foundation of China (12202042), the Fundamental Research Funds for the Central Universities (QNXM20220011, FRF-TP-22-119A1, FRF-IDRY-22-001), the Open Fund Project of Sinopec State Key Laboratory of Shale Oil and Gas Enrichment Mechanisms and Effective Development (33550000-22-ZC0613-0269), China Postdoctoral Science Foundations (2021M700391), and High-end Foreign Expert Introduction Program (G2023105006L).

Appendix A. Equation derivation

The continuity equation within the primary fracture system can be given as

$$-\mathrm{div}(\rho \nu_{\mathrm{F}}) + \frac{\rho_{\mathrm{Sc}} q_{\mathrm{F}}}{\omega_{\mathrm{E}} h} + \frac{\rho_{\mathrm{Sc}} q_{\mathrm{F}}}{\omega_{\mathrm{E}} h} \delta(r) = 0 \tag{A-1}$$

The motion equation with stress sensitivity is

$$v_{\rm F} = \frac{k_{\rm Fi} e^{-\alpha(p_i - p)}}{\mu} \frac{\partial p}{\partial r} \tag{A-2}$$

where the subscript i represents the initial state. The continuity equation within secondary fracture systems in divergence form is

$$-\text{div}(\rho v) - q_{\text{m}} = \frac{\partial(\rho\phi)}{\partial t} \tag{A-3}$$

where q_m is the fluid volume of fluid channeling. The state equation of shale gas is

$$\rho = \frac{pM_{\rm g}}{ZRT} \tag{A-4}$$

The definition of improved permeability modulus and pseudopressure are

$$\alpha' = \frac{\mu Z}{2n} \alpha \tag{A-5}$$

$$m = \int_{p_{c}}^{p} \frac{2p}{\mu Z} dp \tag{A-6}$$

With Fick's diffusion law, the motion equation in shale matrix can be presented as

$$v_{\rm m} = D \frac{\partial V}{\partial r_{\rm m}} \tag{A-7}$$

The equation of continuity in the matrix can be expressed as

$$-\operatorname{div}(\rho_{sc}\nu_{m}) = q_{m} \tag{A-8}$$

The gas adsorption in the shale matrix is assumed to satisfy Langmuir isotherm and the shale gas concentration at the surface and initial state of the matrix unit can be written as

$$V_{\rm e} = V_{\rm L} \frac{p}{p_{\rm L} + p} \tag{A-9}$$

$$V_i = V_L \frac{p_i}{p_L + p_i} \tag{A-10}$$

The definition of permeability modulus is

$$a = \frac{3.684 \times 10^{-3} \mu Z p_{sc} q_{sc} T}{K_i h T_{sc}} \frac{V_L p_L}{(p_L + p)(p_L + p_i)(p + p_i)}$$
(A-11)

After perturbation transformation, the Taylor expansion for pressure can be written as

$$m_{\rm D} = \xi_{\rm D} + \frac{1}{2}\alpha_{\rm D}\xi_{\rm D}^2 + ... = -\frac{1}{\alpha_{\rm D}}\ln(1 - \alpha_{\rm D}\xi_{\rm D})$$
 (A-12)

Appendix B. Dimensionless parameters

The dimensionless pressure is given as

$$m_{\rm D} = \frac{k_{\rm fi}T_{\rm sc}h(m_{\rm i}-m)}{3.684\times 10^{-3}p_{\rm sc}q_{\rm sc}T} \tag{B-1}$$

The dimensionless time is

$$t_{\rm D} = \frac{3.6k_{\rm fi}t}{\mu h^2} \frac{1}{\left(\varphi C_{\rm g}\right)_{\rm f+m} + \frac{k_{\rm fi}h}{1.842 \times 10^{-3}q_{\rm sc}\mu}} \tag{B-2}$$

The dimensionless stress sensitive coefficient is

$$\alpha_{\rm D} = \frac{3.684 \times 10^{-3} p_{\rm sc} q_{\rm sc} T}{k_{\rm fi} T_{\rm sc} h} \alpha \tag{B-3}$$

The dimensionless diffusion coefficient is

$$D_{\rm D} = \frac{D\mu h^2}{3.6k_{\rm fi}R_{\rm m}^2} \times \left((\varphi C_{\rm g})_{\rm f+m} + \frac{k_{\rm fi}h}{1.842 \times 10^{-3}q_{\rm sc}\mu} \right) \tag{B-4}$$

The definition of adsorption index is

$$a = \frac{3.684 \times 10^{-3} \mu Z p_{sc} q_{sc} T}{2 k_{fi} h T_{sc}} \frac{V_L p_L}{(p_L + p)(p_L + p_i)(p + p_i)} \tag{B-5} \label{eq:B-5}$$

The storage ratio is given as

$$\omega = \frac{(\varphi C_{\rm g})_{\rm f}}{(\varphi C_{\rm g})_{\rm f+m} + \frac{k_{\rm fi}h}{1.842 \times 10^{-3} q_{\rm sc}\mu}}$$
(B-6)

The dimensionless primary fracture conductivity is

$$C_{\rm FD} = \frac{k_{\rm F} w_{\rm F}}{k_{\rm B} h} \tag{B-7}$$

The dimensionless formation thickness is

$$h_{\rm D} = \frac{h}{I} \tag{B-8}$$

The dimensionless distance is

$$r_{\rm D} = \frac{r}{I} \tag{B-9}$$

The dimensionless well spacing is given as

$$W_{\rm D} = \frac{W}{I} \tag{B-10}$$

where *L* is the reference length; *h* is the formation thickness.

References

- Abdelaziz, A., Ha, J., Li, M., Magsipoc, E., Sun, L., Grasselli, G., 2023. Understanding hydraulic fracture mechanisms: from the laboratory to numerical modelling. Advances in Geo-Energy Research 7 (1), 66–68. https://doi.org/10.46690/ ager.2023.01.07.
- Al-Shami, T.M., Jufar, S.R., Kumar, S., Abdulelah, H., Abdullahi, M.B., Al-Hajri, S., Negash, B.M., 2023. A comprehensive review of interwell interference in shale reservoirs. Earth Sci. Rev. 237, 104327. https://doi.org/10.1016/j.earscirev.2023.104327.
- Altman, R., Tineo, R., Viswanathan, A., Gurmen, N., 2020. Applied learnings in reservoir simulation of unconventional plays. In: SPE Latin American and Caribbean Petroleum Engineering Conference. https://doi.org/10.2118/199164-MS
- Arif, M., Mahmoud, M., Zhang, Y., Iglauer, S., 2021. X-ray tomography imaging of shale microstructures: a review in the context of multiscale correlative imaging. Int. J. Coal Geol. 233, 103641. https://doi.org/10.1016/j.coal.2020.103641.
- Bellani, J., Verma, H.K., Khatri, D., Makwana, D., Shah, M., 2021. Shale gas: a step toward sustainable energy future. J. Pet. Explor. Prod. Technol. 11, 2127–2141. https://doi.org/10.1007/s13202-021-01157-7.
- Chen, B., Barboza, B.R., Sun, Y., et al., 2021. A review of hydraulic fracturing simulation. Arch. Comput. Methods Eng. 29, 1–58. https://doi.org/10.1007/s11831-021-09653-z.

Chen, Z., Liao, X., Zhao, X., Dou, X., Zhu, L., 2015. Performance of horizontal wells with fracture networks in shale gas formation. J. Petrol. Sci. Eng. 133, 646–664. https://doi.org/10.1016/j.petrol.2015.07.004.

Petroleum Science 22 (2025) 1155-1170

- Chu, H., Dong, P., Lee, W.J., 2023a. A deep-learning approach for reservoir evaluation for shale gas wells with complex fracture networks. Advances in Geo-Energy Research 7 (1), 49–65. https://doi.org/10.46690/ager.2023.01.06.
- Chu, H., Ma, T., Zhu, W., Gao, Y., Zhang, J., Lee, W.J., 2023b. A novel semi-analytical monitoring model for multi-horizontal well system in large-scale underground natural gas storage: methodology and case study. Fuel 334, 126807. https://doi.org/10.1016/j.fuel.2022.126807.
- Coley, C., Rincones, M.D., Wiggs, K., Prabowo, W., 2023. Empirical and semianalytical workflow to determine optimal spacing in unconventional reservoirs. In: Unconventional Resources Technology Conference. https://doi.org/ 10.15530/urtec-2023-3855657
- Cui, Q., Zhao, Y., Zhang, L., Chen, M., Gao, S., Chen, Z., 2023. A semianalytical model of fractured horizontal well with hydraulic fracture network in shale gas reservoir for pressure transient analysis. Advances in Geo-Energy Research 8 (3). https://doi.org/10.46690/ager.2023.06.06.
- Dahim, S., Taghavinejad, A., Razghandi, M., Rigi, H.R., Moeini, K., Jamshidi, S., Sharifi, M., 2020. Pressure and rate transient modeling of multi fractured horizontal wells in shale gas condensate reservoirs. J. Petrol. Sci. Eng. 185, 106566. https://doi.org/10.1016/j.petrol.2019.106566.
- Damjanac, B., Detournay, C., Cundall, P., 2020. Numerical simulation of hydraulically driven fractures. Modelling Rock Fracturing Processes: Theories, Methods, and Applications 531–561. https://doi.org/10.1007/978-3-030-35525-8_20.
- Du, X., Li, Q., Xian, Y., Lu, D., 2021. Fully implicit and fully coupled numerical scheme for discrete fracture modeling of shale gas flow in deformable rock. J. Petrol. Sci. Eng. 205, 108848. https://doi.org/10.1016/j.petrol.2021.108848.
- Ehlig-Economides, C., de Guzman, N., 2020. Cost comparison between carbon neutral fuel and alternative low carbon energy options. In: SPE Annual Technical Conference and Exhibition. https://doi.org/10.2118/201613-MS.
- Farah, N., Delorme, M., 2020. Unified fracture network model (UFNM) for unconventional reservoirs simulation. J. Petrol. Sci. Eng. 195, 107874. https://doi.org/10.1016/j.petrol.2020.107874.
- Fiallos Torres, M.X., Yu, W., Ganjdanesh, R., Kerr, E., Sepehrnoori, K., Miao, J., Ambrose, R., 2019. Modeling interwell fracture interference and Huff-N-Puff pressure containment in eagle ford using EDFM. In: SPE Oklahoma City Oil and Gas Symposium. https://doi.org/10.2118/195240-MS.
- and Gas Symposium. https://doi.org/10.2118/195240-MS.
 Gou, Q., Xu, S., Hao, F., et al., 2020. Quantitative calculated shale gas contents with different lithofacies: a case study of Fuling gas shale, Sichuan Basin, China.
 J. Nat. Gas Sci. Eng. 76, 103222. https://doi.org/10.1016/j.jngse.2020.103222.
- Guo, X., 2019. Major factors controlling the shale gas accumulations in wufenglongmaxi formation of the pingqiao shale gas field in fuling area, Sichuan Basin, China. Journal of Natural Gas Geoscience 4 (3), 129–138. https://doi.org/10.1016/j.jnggs.2019.06.002.
- Guo, X., Hu, D., Shu, Z., et al., 2023. Exploration, development, and construction in the Fuling national shale gas demonstration area in Chongqing: progress and prospects. Nat. Gas. Ind. B 10 (1), 62–72. https://doi.org/10.1016/ j.ngib.2023.01.009.
- Haghshenas, B., Qanbari, F., 2021. Analysis of pressure interference tests in unconventional gas reservoirs: a gas condensate example from montney formation. In: SPE Hydraulic Fracturing Technology Conference and Exhibition. https://doi.org/10.2118/204161-MS.
- Hamdi, H., Behmanesh, H., Clarkson, C.R., 2021. A simple method for quantifying inter-well communication using production data from single-phase shale gas reservoirs. In: SPE Annual Technical Conference and Exhibition. https://doi.org/ 10.2118/205839-MS.
- Jalali, Y., Ershaghi, I., 1987. Pressure transient analysis of heterogeneous naturally fractured reservoirs. In: SPE California Regional Meeting. https://doi.org/ 10.2118/16341-MS.
- Jin, Z., 2023. Hydrocarbon accumulation and resources evaluation: recent advances and current challenges. Advances in Geo-Energy Research 8 (1), 1–4. https:// doi.org/10.46690/ager.2023.04.01.
- Kanwal, S., Mehran, M.T., Hassan, M., Anwar, M., Naqvi, S.R., Khoja, A.H., 2022. An integrated future approach for the energy security of Pakistan: replacement of fossil fuels with syngas for better environment and socio-economic development. Renew. Sustain. Energy Rev. 156, 111978. https://doi.org/10.1016/irser.2021.111978
- Kurotori, T., Murugesu, M.P., Zahasky, C., Vega, B., Druhan, J.L., Benson, S.M., Kovscek, A.R., 2023. Mixed imbibition controls the advance of wetting fluid in multiscale geological media. Adv. Water Resour. 175, 104429. https://doi.org/ 10.1016/j.advwatres.2023.104429.
- Liu, Q., Tian, S., Yu, W., Li, G., Sheng, M., Sepehrnoori, K., Wang, T., 2020. A semi-analytical model for simulation of multiple vertical wells with well interference. J. Petrol. Sci. Eng. 195, 107830. https://doi.org/10.1016/i.petrol.2020.107830.
- Micheal, M., Xu, W., Xu, H., Zhang, J., Jin, H., Yu, H., Wu, H., 2021. Multi-scale modelling of gas transport and production evaluation in shale reservoir considering crisscrossing fractures. J. Nat. Gas Sci. Eng. 95, 104156. https:// doi.org/10.1016/j.jngse.2021.104156.
- Micheal, M., Xu, W., Jin, J., Yu, H., et al., 2022. A multi-scale quadruple-continuum model for production evaluation of shale gas reservoirs considering complex gas transfer mechanisms and geomechanics. J. Petrol. Sci. Eng. 213, 110419. https://doi.org/10.1016/j.petrol.2022.110419.
- Miller, G., Lindsay, G., Baihly, J., Xu, T., 2016. Parent well refracturing: economic

- safety nets in an uneconomic market. In: SPE Low Perm Symposium. https://doi.org/10.2118/180200-MS.
- Molina, O.M., 2019. Analytical model to estimate the fraction of frac hits in multiwell pads. In: Unconventional Resources Technology Conference. https:// doi.org/10.15530/urtec-2019-238.
- Nie, H., Li, D., Liu, G., Lu, Z., Hu, W., Wang, R., Zhang, G., 2020. An overview of the geology and production of the Fuling shale gas field, Sichuan Basin, China. Energy Geoscience 1 (3–4), 147–164. https://doi.org/10.1016/j.engeos.2020.06.005.
- Nie, H., Jin, Z., Li, P., et al., 2023. Deep shale gas in the Ordovician-Silurian Wufeng—Longmaxi formations of the Sichuan Basin, SW China: insights from reservoir characteristics, preservation conditions and development strategies. J. Asian Earth Sci. 244, 105521. https://doi.org/10.1016/j.jseaes.2022.105521.
- Ozkan, E., 2023. Pressure-and rate-transient model for an array of interfering fractured horizontal wells in unconventional reservoirs. SPE J. 29 (8), 4194–4217. https://doi.org/10.2118/215031-PA.
- Pang, W., Ehlig-Economides, C.A., Du, J., He, Y., Zhang, T., 2015. Effect of well interference on shale gas well SRV interpretation. In: SPE Asia Pacific Unconventional Resources Conference and Exhibition. https://doi.org/10.2118/176910-MS.
- Pedrosa, Jr O.A., 1986. Pressure transient response in stress-sensitive formations. In: SPE California Regional Meeting. https://doi.org/10.2118/15115-MS.
- Rivera, S., Shin, Y., 2023. Understanding the advantages and disadvantages of unconventional well stacking and interference. In: Unconventional Resources Technology Conference. https://doi.org/10.15530/urtec-2023-3866237.
- Sherratt, J., Haddad, A.S., Wejzerowski, F., Rafati, R., 2021. Optimising well orientation in hydraulic fracturing of naturally fractured shale gas formations. J. Nat. Gas Sci. Eng. 94, 104141. https://doi.org/10.1016/j.jngse.2021.104141.
- Singh, H., Javadpour, F., 2016. Langmuir slip-Langmuir sorption permeability model of shale. Fuel 164, 28–37. https://doi.org/10.1016/j.fuel.2015.09.073.
- Sobecki, N., Wang, S., Ding, D.Y., Nieto-Draghi, C., Wu, Y.S., 2020. A multi-scale modeling of confined fluid: from nanopore to unconventional reservoir simulation. J. Petrol. Sci. Eng. 193, 107364. https://doi.org/10.1016/j.petrol.2020.107364.
- Soulaine, C., Creux, P., Tchelepi, H.A., 2019. Micro-continuum framework for porescale multiphase fluid transport in shale formations. Transport Porous Media 127, 85–112. https://doi.org/10.1007/s11242-018-1181-4.
- Spivey, J.P., Lee, W.J., 1998. New solutions for pressure transient response for a

- horizontal or a hydraulically fractured well at an arbitrary orientation in an anisotropic reservoir. In: SPE Annual Technical Conference and Exhibition. https://doi.org/10.2118/49236-MS.
- Stehfest, H., 1970. Algorithm 368: numerical inversion of Laplace transforms [D5]. Commun. ACM 13 (1), 47–49.
- Taghavinejad, A., Sharifi, M., Heidaryan, E., Liu, K., Ostadhassan, M., 2020. Flow modeling in shale gas reservoirs: a comprehensive review. J. Nat. Gas Sci. Eng. 83, 103535. https://doi.org/10.1016/j.jngse.2020.103535.
- Takbiri-Borujeni, A., Fathi, E., Kazemi, M., Belyadi, F., 2019. An integrated multiscale model for gas storage and transport in shale reservoirs. Fuel 237, 1228—1243. https://doi.org/10.1016/i.fuel.2018.10.037.
- Thomas, L., Tang, H., Kalyon, D.M., et al., 2019. Toward better hydraulic fracturing fluids and their application in energy production: a review of sustainable technologies and reduction of potential environmental impacts. J. Petrol. Sci. Eng. 173, 793–803. https://doi.org/10.1016/j.petrol.2018.09.056.
- Torres, M.F., Morales, A., Yu, W., Miao, J., 2021. Characterization of complex hydraulic fractures in Eagle Ford shale oil development through embedded discrete fracture modeling. Petrol. Explor. Dev. 48 (3), 713–720. https://doi.org/10.1016/51876-3804(21)60057-5.
- Wang, P., Su, P., Fan, H., Kong, X., Jia, Y., 2021. Inter-well interference analysis and well spacing optimization for multi-stage fractured horizontal wells of shale gas reservoirs based on multi-information. In: International Field Exploration and Development Conference. https://doi.org/10.1007/978-981-19-2149-0_10.
- Yang, X., Yu, W., Wu, K., Weijermars, R., 2020. Assessment of production interference level due to fracture hits using diagnostic charts. SPE J. 25 (6), 2837–2852. https://doi.org/10.2118/200485-PA
- Yang, Y., Liu, S., 2020. Review of shale gas sorption and its models. Energy Fuels 34 (12), 15502–15524. https://doi.org/10.1021/acs.energyfuels.0c02906.
- Zheng, H., Pu, C., Xu, E., Sun, C., 2020. Numerical investigation on the effect of well interference on hydraulic fracture propagation in shale formation. Eng. Fract. Mech. 228, 106932. https://doi.org/10.1016/j.engfracmech.2020.106932.
- Zhu, C., Wang, J., Sang, S., Liang, W., 2023. A multiscale neural network model for the prediction on the equivalent permeability of discrete fracture network. J. Petrol. Sci. Eng. 220, 111186. https://doi.org/10.1016/j.petrol.2022.111186.
- Zou, C., Pan, S., Hao, Q., 2020. On the connotation, challenge and significance of China's "energy independence" strategy. Petrol. Explor. Dev. 47 (2), 416–426. https://doi.org/10.11698/PED.2020.02.21.